Brief Communication

Rapid biomechanical imaging at low irradiation level via dual line-scanning Brillouin microscopy

Jitao Zhang [1,2,5] ✉, Milos Nikolic [1,3,4,5], Kandice Tanner[4] & Giuliano Scarcelli [1,3] ✉

Brillouin microscopy is a technique for mechanical characterization of biological material without contact at high three-dimensional resolution. Here, we introduce dual line-scanning Brillouin microscopy (dLSBM), which improves acquisition speed and reduces irradiation dose by more than one order of magnitude with selective illumination and single-shot analysis of hundreds of points along the incident beam axis. Using tumor spheroids, we demonstrate the ability to capture the sample response to rapid mechanical perturbations as well as the spatially resolved evolution of the mechanical properties in growing spheroids.

The biomechanical properties and interactions of cells and tissues are critically involved in many biological functions[1,2]. As a result, many techniques have been developed in the past decades to quantify the mechanical properties of biologically relevant materials[3,4]. Of these, Brillouin optical microscopy has emerged as an attractive option due to its ability to probe material mechanics without contact or labels[5–7]. Thus, Brillouin microscopy can provide mechanical measurements when traditional methods cannot be used, for example because no physical access can be gained to the region of interest such as in tissue[8], three-dimensional (3D) microenvironments[9] or microfluidic channels[10].

Spontaneous Brillouin scattering arises when light interacts with thermal acoustic phonons (that is, quanta of vibrational energy), resulting in scattered light[11]. The Brillouin frequency shift, that is, the difference in frequency between the incident and scattered light (~0.01 nm), is related to the longitudinal elastic modulus and thus can provide information on the local mechanical properties of the material. Despite tremendous progress in confocal Brillouin microscopy over the past 15 years, slow acquisition speed (20–200 ms per spectrum) remains the major limiting factor in the widespread adoption of Brillouin technology in biomedicine[12]. To overcome the speed limitation, stimulated Brillouin scattering has been recently proposed[13], in which acoustic phonons are driven by a resonant pump–probe interaction so that a stronger Brillouin signal is generated. However, stimulated Brillouin

spectrometers have not reduced acquisition time below 20 ms in biological samples due to sub-optimal continuous wave operation and less efficient light detection. In addition, both spontaneous and stimulated Brillouin microscopy are based on point-scanning, leading to slow acquisition speeds and high irradiation doses due to the redundant illumination of out-of-focus voxels.

An efficient solution to the speed–photodamage challenge lies in multiplexing. For example, light-sheet fluorescence microscopy has improved acquisition speed and reduced photodamage in confocal fluorescence microscopy by selective illumination and multiplexed detection[14]. Here, we developed a multiplexing solution for Brillouin spectroscopy–microscopy via dual line-scanning Brillouin microscopy (dLSBM) with simultaneous imaging and single-shot spectral analysis of hundreds of points. The set-up features dual line illumination with counterpropagating beams that are sequentially switched on (Fig. 1a,b and Extended Data Fig. 1), which enables light-efficient multiplexing along the illumination axis and orthogonal collection free of refractive index artifacts (Supplementary Note 1 and Extended Data Figs. 2 and 3). To enable single-shot Brillouin spectral analysis of the multiple points, we used the perpendicular direction to the dispersion axis of an etalon interferometer[15] for spatial multiplexing. Furthermore, to minimize absorption-induced phototoxicity we used a narrow-band infrared laser and cleaned its spectrum to suppress side modes and amplified

[1]Fischell Department of Bioengineering, University of Maryland, College Park, MD, USA. [2]Department of Biomedical Engineering, Wayne State University, Detroit, MI, USA. [3]Maryland Biophysics Program, University of Maryland, College Park, MD, USA. [4]Laboratory of Cell Biology, Center for Cancer Research, National Cancer Institute, National Institutes of Health, Bethesda, MD, USA. [5]These authors contributed equally: Jitao Zhang, Milos Nikolic. ✉e-mail: zhang4@wayne.edu; scarc@umd.edu
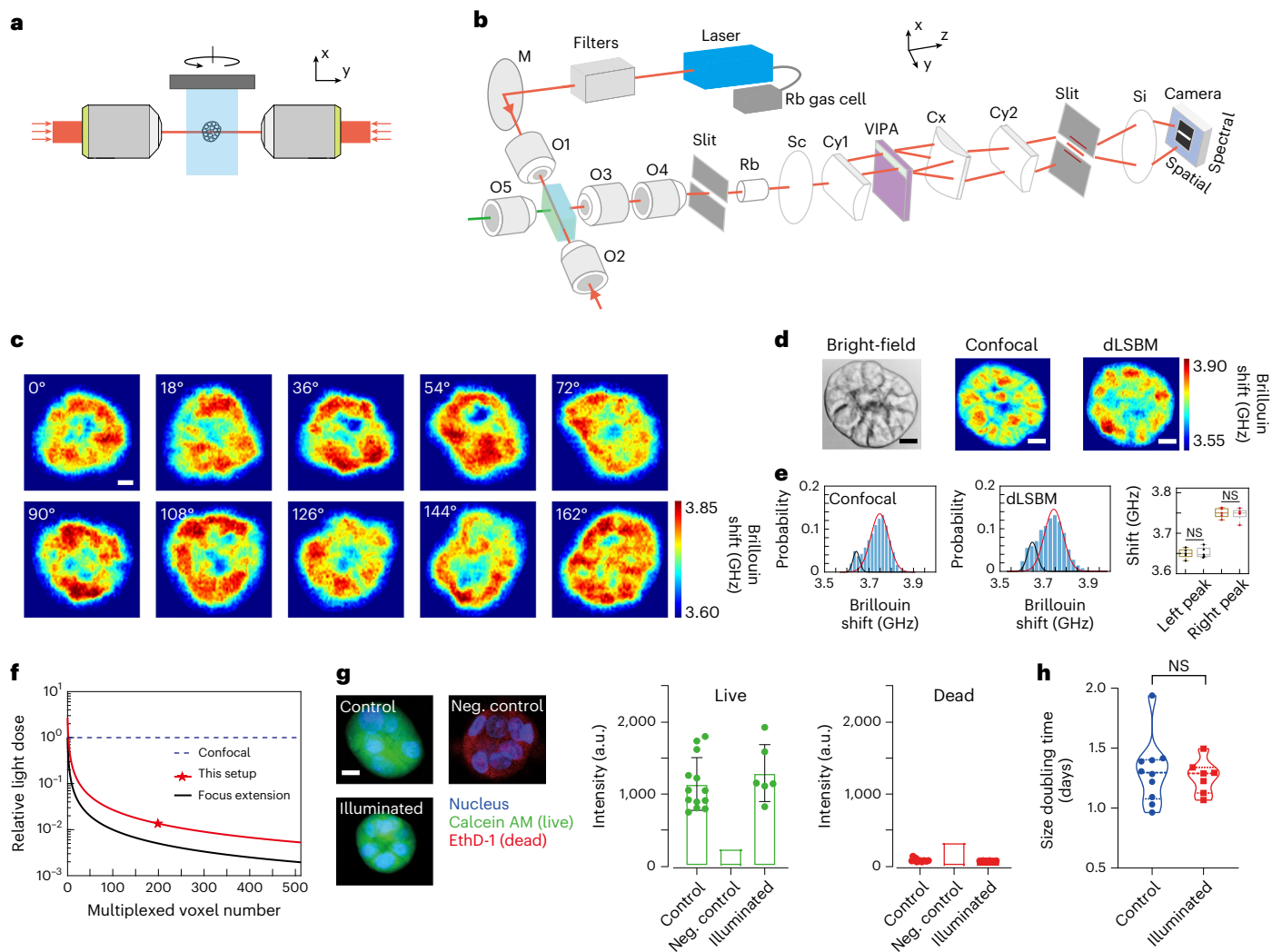
Fig. 1 | Design and validation of dLSBM. a, Schematic diagram of the dual-line illumination configuration. **b**, Optical set-up of the instrument. The laser beam, the frequency of which is locked to the absorption line of rubidium gas, is spectrally cleaned by filters and focused into the sample from two sides. A home-built bright-field microscope (indicated by the green line and O5) is used for image guidance and alignment of the laser beam, and the Brillouin signals are collected by the multiplexed spectrometer. Cy1, Cy2, Cx, cylindrical lenses; M, mirror; O1–O5, objective lenses; Rb, rubidium gas chamber; Sc, Si, spherical lenses; VIPA, virtually imaged phased array. **c**, 3D Brillouin mapping of a spheroid by rotating it along the x axis. Labels indicate the relative azimuth angle in the $y–z$ plane. $100 \times 200 \times 10$ pixels were scanned, with a total acquisition time of less than 4 min. **d**, Brillouin images of the same spheroid measured by confocal Brillouin modality at 180° scattering geometry (that is, the angle between the illumination light and the scattered light) and the dLSBM at 90° scattering geometry. The acquisition time for each image (100×200 pixels) in dLSBM and confocal Brillouin microscopy is ~20 s and 16 min, respectively. **e**, Histogram distributions of the Brillouin shifts of the scanned sections by confocal Brillouin microscopy and dLSBM. The solid lines are the fitting results by Gaussian profile.

In the right-hand graph the locations of the left and right peak are 3.643 GHz and 3.747 GHz for the confocal image (gold) and 3.646 GHz and 3.744 GHz for the line-scanning image (dark gray), respectively. Multiple independent spheroids ($n = 5$) were measured, and there was no significant difference in the peak positions. Statistical significance was determined using a two-sided two-sample t-test (left peak: $P = 0.7758$; right peak: $P = 0.7303$). In all boxplots, the central horizontal indicates the median, and the bottom and top edges of the boxes indicate the 25th and 75th percentiles, respectively. The whiskers extend to the most extreme data points not considered outliers. **f**, Induced light dose of the dLSBM set-up compared with the confocal configuration for 3D Brillouin imaging. **g**, Live–dead assay. Control group, $n = 13$; illuminated group, $n = 6$; the negative control was used for calibrating the fluorescence intensity of the red channel, $n = 1$. EthD-1, ethidium homodimer-1. The bars represents the mean, and the error bars represent standard deviation. **h**, Comparison of the proliferation rate between control ($n = 10$) and illuminated ($n = 7$) spheroids. NS, not significant ($P = 0.7180$). Statistical significance was determined using the two-sided unpaired t-test. Scale bars, 10 μm.

spontaneous emission (Extended Data Fig. 1, Methods). Using such a laser also enabled an additional 40 dB rejection of non-Brillouin light with a heated rubidium gas cell. Overall, the multiplexed Brillouin spectrometer reaches the required specifications for biomechanical analysis of biological samples (Extended Data Fig. 4a–g): spectral extinction >70 dB for shot noise operation; spectral resolution of 0.25 GHz and spectral precision of 10 MHz; and equivalent acquisition of 1 ms per pixel in biological samples, which is more than one order

of magnitude faster than state-of-the-art spontaneous confocal or stimulated set-ups[12,13].

To acquire a 3D image, multiple two-dimensional (2D) Brillouin images were taken by rotating the spheroid in the $y–z$ plane with a total acquisition time of ~4 minutes (Fig. 1c and Extended Data Fig. 5). Overall, using an illumination numerical aperture of 0.1 and a collection numerical aperture of 0.3, the dLSBM has a spatial resolution of 1.6 μm × 1.6 μm × 4.0 μm (Extended Data Fig. 6) and a field of view of
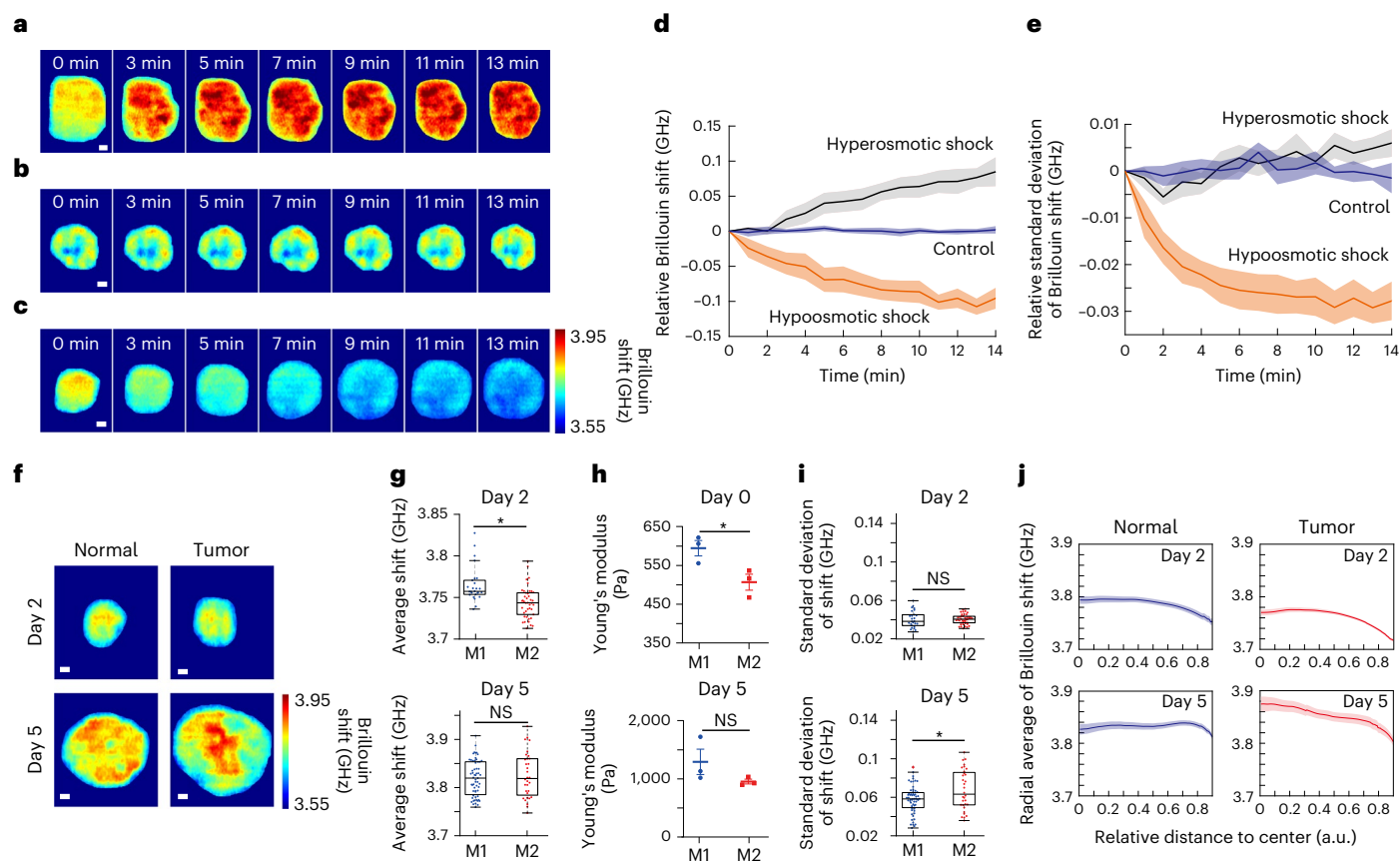
Fig. 2 | Mechanical response of the spheroids to external perturbations and long-term mechanical evolution. a–c, Representative time-lapse Brillouin images of the spheroid under conditions of hyperosmotic shock (**a**), no shock (**b**) and hypoosmotic shock (**c**). A total of 100 × 200 pixels were scanned for each image, with the acquisition speed of 20 s per frame. Scale bars, 10 μm. **d,e**, Temporal change of the average Brillouin shift (**d**) and the standard deviation (**e**) of spheroids in the hyperosmotic shock group ($n = 5$), the control group ($n = 6$) and the hypoosmotic shock group ($n = 5$). **f**, Representative Brillouin images of spheroids from a healthy cell line (M1) and from a tumor cell line (M2) on day 2 and day 5. Scale bar, 10 μm. **g**, Brillouin shift of M1 ($n = 26$) and M2 ($n = 42$) on day 2 and M1 ($n = 59$) and M2 ($n = 32$) on day 5. Day 2, *$P = 5 \times 10^{-5}$; day 5, not significant (NS; $P = 0.4817$). Statistical significance was determined using the two-sided two-sample t-test with no adjustments. **h**, Young's modulus of M1 and M2 on days 0 and 5, as measured using atomic force microscopy (AFM). The mean ± s.e.m. are determined for $n = 3$ independent experiments. Day 0, *$P = 0.0379$; day 5, NS ($P = 0.2023$). Statistical significance was determined using the two-sided unpaired t-test. **i**, Standard deviation of the Brillouin shift of M1 and M2. Day 2, NS ($P = 0.9493$); day 5, *$P = 0.0074$. Statistical significance was determined using the two-sided two-sample t-test with no adjustments. **j**, Radial average of the Brillouin shifts of normal and tumor spheroids on day 2 and day 5. Plot with error band represents the mean ± s.e.m. In all boxplots, the central horizontal line indicates the median, and the bottom and top edges indicate the 25th and 75th percentiles, respectively. The whiskers extend to the most extreme data points not considered outliers.

150 μm × 150 μm × 160 μm. For validation, we compared our dLSBM set-up with a confocal Brillouin microscope using the same spheroid sample (Fig. 1d and Extended Data Fig. 7). Although the co-registration of images cannot be exact because the voxel size of dLSBM is twofold smaller and the sample is manually transferred between instruments, the histogram distributions of the images indicate that dLSBM captured the same mechanical features as the confocal Brillouin microscope (Fig. 1e). With nuclear staining of the spheroids, we confirmed that the right peaks of the histograms were dominated by the Brillouin shift of the cell nuclei (Extended Data Fig. 8), indicating that dLSBM probes spheroid mechanics at subcellular resolution.

Given that spontaneous Brillouin scattering operates in a non-depleted-pump condition, and thanks to the dual line illumination (Supplementary note 1), we could implement 'on-axis' multiplexing, that is, the illumination beam propagation axis is the multiplexing direction. This eliminates the out-of-focus redundant illumination of point-scanning or off-axis multiplexing configurations, and thus results in the total light dose being reduced to 7.4% of an equivalent confocal set-up (Fig. 1f, red star) for 3D imaging (Supplementary Note 2 and Extended Data Fig. 4h). The application of focus-extension techniques

could further reduce the light dose by fivefold (Fig. 1f, black curve). As well as the avoidance of photodamage (Fig. 1g), the dLSBM light dose importantly does not affect spheroid growth (Fig. 1h and Extended Data Fig. 9), a clear demonstration of the non-perturbative nature of the configuration. In summary, dLSBM provides an improvement of more than one order of magnitude in both acquisition speed and light dose, thus enabling Brillouin imaging for both rapid response and long-term biomechanical studies.

Tumor organoids are a valuable field-testing sample because they represent a widespread model to study tumor etiology, progression and drug sensitivity[16], the mechanical properties of which have remained elusive[17]. The improved acquisition speed of the dLSBM enabled us to monitor the quick mechanical response of tumor spheroids to osmotic stress[18]. We subjected tumor spheroids to osmotic shocks and tracked their Brillouin shift every minute (Fig. 2a–c). As expected, the Brillouin shift of the multicellular spheroids increased under hyperosmotic shock and decreased under hypoosmotic shock (Fig. 2d and Extended Data Fig. 10). Brillouin imaging also showed that the internal mechanical heterogeneity responded differently to hyperosmotic shocks, in which spheroids maintained a similar spatial heterogeneity

to control samples, compared with hypoosmotic shocks, in which the spheroids became spatially uniform (Fig. 2e and Supplementary Fig. 1): this is expected given that the modulus behavior flattens with increasing hydration, but may also be exacerbated by the diminished sensitivity of the Brillouin technique at high hydration levels[19].

Recent work has shown that the mechanical properties of tumor cells as a function of the extracellular matrix milieu are different from those of their normal counterparts[20]. However, what drives this mechanical coupling across multicellular structures is less understood. This is an open question with regard to how tumor cells adapt to mechanical environments along the metastatic cascade. Here, using spheroids derived from breast cancer isogenic cancer progression lines that mimic different stages of malignancy, we used dLSBM to compare the mechanical evolution of healthy tissue spheroids (from a healthy epithelial cell line, that is, M1: MCF10A) with the mechanical properties of tumor-like tissue spheroids (from a tumor cell line, that is, M2: MCF10AT1k.cl2). At the single-cell level, healthy mammary cells have a higher modulus than the corresponding precancerous or cancerous ones[21]; here, we investigated whether such a relation was conserved with spheroid growth. We measured spheroids at an early (day 2) and a later (day 5) culturing stage (Fig. 2f and Supplementary Fig. 2). At day 2, tumor spheroids had a lower Brillouin shift than healthy spheroids, mirroring the single-cell behavior. However, as spheroids grew, this mechanical difference vanished (Fig. 2g), an observation that we validated with atomic force microscopy (Fig. 2h and Supplementary Fig. 3). Beyond average values, dLSBM enables investigation of the spatial behavior of the mechanical evolution of multicellular spheroids. We observed that the tumor spheroids had higher mechanical heterogeneity than normal ones while growing (Fig. 2i). To further understand this feature, we extracted the radial average of the Brillouin shift (Fig. 2j). We found that both normal and tumor spheroids had a similar radial mechanical change in the early stages. At later stages, however, the tumor population had a much steeper radial gradient than the normal spheroids, suggesting that the change in mechanical properties is driven by the core of the spheroids. Given that tumor progression is often accompanied by altered tissue biomechanics, dLSBM can serve as a unique platform to dissect the role of mechanical regulation in tumorigenesis.

Here, we have demonstrated rapid 3D mechanical mapping of biological samples using dLSBM, which features simultaneous imaging and single-shot spectral analysis of hundreds of points along the optical axis. Compared with previous line scan spectrometer design[15], dLSBM has >1,000-fold higher spectral extinction, ~80-fold lower photodamage and long-term stability in longitudinal biological experiments enabled by laser frequency locking. Further improvements in our technique include focus extension of the illumination beam, inverted geometry for easier and flexible sample preparation, greater penetration depth via adaptive optics and the combination of dLSBM and light-sheet fluorescence microscopy. We validated the technique against confocal Brillouin microscopy to verify the equivalence of the extracted information and the superior performance in terms of speed and light dose. We showed that dLSBM can detect biologically relevant mechanical changes in multicellular organisms such as tumor spheroids in both short-term studies and long-term culture, limited only by the penetration depth of the illumination beam due to spheroid turbidity. Consistent with previous studies[17,22], we observed a robust stiffening behavior in the evolution of growing tumor spheroids, which we validated against gold standard atomic force microscopy. These capabilities show that dLSBM is a promising method for the study of biomechanical processes in developmental biology, tissue engineering and organ-on-a-chip applications.

Online content

Any methods, additional references, Nature Portfolio reporting summaries, source data, extended data, supplementary information, acknowledgements, peer review information; details of author contributions and competing interests; and statements of data and code availability are available at https://doi.org/10.1038/s41592-023-01816-z.

References

1. Wang, N., Tytell, J. D. & Ingber, D. E. Mechanotransduction at a distance: mechanically coupling the extracellular matrix with the nucleus. *Nat. Rev. Mol. Cell Biol.* **10**, 75–82 (2009).
2. Miller, C. J. & Davidson, L. A. The interplay between cell signalling and mechanics in developmental processes. *Nat. Rev. Genet.* **14**, 733–744 (2013).
3. Bao, G. & Suresh, S. Cell and molecular mechanics of biological materials. *Nat. Mater.* **2**, 715–725 (2003).
4. Kennedy, B. F., Wijesinghe, P. & Sampson, D. D. The emergence of optical elastography in biomedicine. *Nature Photonics* **11**, 215–221 (2017).
5. Scarcelli, G. et al. Noncontact three-dimensional mapping of intracellular hydromechanical properties by Brillouin microscopy. *Nat. Methods* **12**, 1132–1134 (2015).
6. Prevedel, R., Diz-Muñoz, A., Ruocco, G. & Antonacci, G. Brillouin microscopy: an emerging tool for mechanobiology. *Nat. Methods* **16**, 969–977 (2019).
7. Zhang, J. & Scarcelli, G. Mapping mechanical properties of biological materials via an add-on Brillouin module to confocal microscopes. *Nat. Protoc.* **16**, 1251–1275 (2021).
8. Gouveia, R. M. et al. Assessment of corneal substrate biomechanics and its effect on epithelial stem cell maintenance and differentiation. *Nat. Commun.* **10**, 1496 (2019).
9. Margueritat, J. et al. High-frequency mechanical properties of tumors measured by Brillouin light scattering. *Phys. Rev. Lett.* **122**, 018101 (2019).
10. Wisniewski, E. O. et al. Dorsoventral polarity directs cell responses to migration track geometries. *Sci. Adv.* **6**, eaba6505 (2020).
11. Dil, J. G. Brillouin scattering in condensed matter. *Reports on Progress in Physics* **45**, 285–334 (1982).
12. Antonacci, G. et al. Recent progress and current opinions in Brillouin microscopy for life science applications. *Biophys. Rev.* **12**, 615–624 (2020).
13. Remer, I., Shaashoua, R., Shemesh, N., Ben-Zvi, A. & Bilenca, A. High-sensitivity and high-specificity biomechanical imaging by stimulated Brillouin scattering microscopy. *Nat. Methods* **17**, 913–916 (2020).
14. Huisken, J., Swoger, J., Del Bene, F., Wittbrodt, J. & Stelzer, E. H. Optical sectioning deep inside live embryos by selective plane illumination microscopy. *Science* **305**, 1007–1009 (2004).
15. Zhang, J., Fiore, A., Yun, S.-H., Kim, H. & Scarcelli, G. Line-scanning Brillouin microscopy for rapid non-invasive mechanical imaging. *Sci. Rep.* **6**, 35398 (2016).
16. Tanner, K. & Gottesman, M. M. Beyond 3D culture models of cancer. *Sci. Transl. Med.* **7**, 283ps289 (2015).
17. Han, Y. L. et al. Cell swelling, softening and invasion in a three-dimensional breast cancer model. *Nat. Phys.* **16**, 101–108 (2020).
18. Zhou, E. et al. Universal behavior of the osmotically compressed cell and its analogy to the colloidal glass transition. *Proc. Natl. Acad. Sci. USA* **106**, 10632–10637 (2009).
19. Scarcelli, G. & Yun, S. H. Reply to 'Water content, not stiffness, dominates Brillouin spectroscopy measurements in hydrated materials'. *Nat. Methods* **15**, 562–563 (2018).
20. Taubenberger, A. V. et al. 3D microenvironment stiffness regulates tumor spheroid growth and mechanics via p21 and ROCK. *Adv. Biosyst.* **3**, 1900128 (2019).
21. Cross, S. E., Jin, Y.-S., Rao, J. & Gimzewski, J. K. Nanomechanical analysis of cells from cancer patients. *Nat. Nanotechnol.* **2**, 780–783 (2007).

22. Mahajan, V. et al. Mapping tumor spheroid mechanics in dependence of 3D microenvironment stiffness and degradability by Brillouin microscopy. *Cancers* **13**, 5549 (2021).

Methods

Brillouin light scattering

Brillouin microscopy is based on spontaneous Brillouin scattering, an optical phenomenon caused by the interaction of light and inherent acoustic phonons of the material. The scattered light experiences a frequency shift (that is, Brillouin shift ω_B) determined by the equation $\omega_B = 2n/\lambda \cdot \sqrt{M'/\rho} \cdot \sin(\theta/2)$, where λ is the laser wavelength, n and ρ are the refractive index and density of the material, respectively, M' is the longitudinal modulus, and θ is the collected scattering angle. With a known laser wavelength and scattering geometry, measurements done using Brillouin microscopes with different configurations are directly comparable.

Dual line-scanning Brillouin microscopy

The light source is a continuous wave tunable diode laser (DL pro, Toptica) with a central wavelength of 780.24 nm and a linewidth of less than 0.3 MHz. During operation the laser frequency is locked to the absorption line of rubidium gas (Rb-85), and thus can achieve long-term stability for longitudinal biological study. The light source is coupled to an optical amplifier (BoosTA, Toptica) to generate an output power as high as 3 W. The output beam is delivered to the optical set-up via an optical fiber and a collimator (PAF2A-11B, Thorlabs). The laser spectrum is cleaned using two ultra-narrowband Bragg filters (BP-780, OptiGrate) and a Fabry–Pérot etalon (Light Machinery) with a free spectrum range of 15 GHz. The Bragg filter is very stable and needs few adjustments over a long time period. The Fabry–Pérot etalon has a slow drift that requires optimization within hours. For long-term stabilization, a feedback loop can be built to correct this drift in real time. The laser beam was then expanded to ~9.5 mm and sent into an objective lens (×4/numerical aperture (NA) 0.1, Olympus) to create a loose beam line for illumination. For dual line illumination, a flip mirror is used to guide the beam to create a second identical beam line that propagates against the first one (Extended Data Fig. 1). During measurement the beams are sequentially switched on by the flip mirror. The alignment of the two beams is achieved with the help of a live side image taken by a home-built imaging system, which includes an objective lens (×10/NA 0.25, Olympus), a tube lens (Thorlabs) and an sCMOS (scientific complementary metal–oxide–semiconductor) camera (Neo, Andor). The beam lines were superposed inside a 1 cm cuvette (21-200-255, Fisher Scientific), which was filled with medium and used as the sample holder.

The Brillouin signals generated on the illumination beam line were collected with 90° scattering geometry (that is, the angle between the illumination light and the scattered light) by a multiplexed Brillouin spectrometer (Fig. 1b). To enable simultaneous imaging and spectral analysis, the etalon interferometer is located in the infinity space of a ×2.5 imaging system and the image of the illumination beams is formed at the same plane of the Brillouin spectra. In detail, the beam line was first imaged onto the first slit (VA100, Thorlabs) by a pair of objective lenses (×20/0.4 NA, ×4/0.1 NA, Olympus), which yielded an effective NA of ~0.3 for the collection path. The image of the line was then collimated by a spherical lens (f = 400 mm, Thorlabs) and coupled to the entrance window of the VIPA (virtually imaged phased array) etalon (free spectrum range, 10 GHz; Light Machinery) by a cylindrical lens (f = 200 mm, Thorlabs). After the VIPA etalon, the spectrum of the beam line was projected onto the second slit (VA100, Thorlabs) by a combination of two cylindrical lenses ($f_1 = 1{,}000$ mm, $f_2 = 400$ mm, Thorlabs). The Brillouin spectral pattern was then reimaged by a doublet pair (MAP1040100-B, Thorlabs) and recorded with an EMCCD (electron-multiplying charge-coupled device) camera (iXon Ultra 897, Andor). To improve the spectral extinction, a 150 mm rubidium (Rb) gas cell (TG-ABRB-I85-Q, Precision Glassblowing) was placed between the first slit and the collimation lens, and the laser frequency (780.24 nm) was locked to the Rb-85 absorption line (D_2 hyperfine structure). When heated to around 65 °C, the gas cell can provide spectral extinction of ~40 dB.

A customized four-dimensional stage (three translational movements and one rotational movement) was integrated into the dLSBM set-up for scanning of the sample. We developed a LabVIEW-based program for set-up operation and data acquisition. For spheroid imaging, we used an input laser power of ~370 mW and set the exposure time of the EMCCD to 200 ms. Given that 200 pixels were acquired simultaneously, the equivalent acquisition time for each pixel was 1 ms. The spectral analysis was conducted using MATLAB (R2021b). The Brillouin shift was retrieved by fitting the spectrum with Lorentzian profiles. We used standard materials (that is, water and methanol) for the calibration of the spectrometer.

For dual line illumination imaging, the ultimate image was obtained using the image fusion process in MATLAB. To do this, we adapted a procedure established in light-sheet microscopy[14]. For each sample we first took two Brillouin images under single-line illumination. When the images had observable distortion along the illumination axis, we first used a straight line (perpendicular to the illumination axis) to cut off the portion with distortion. The cut-off location is determined by the overall strength of the Brillouin signal along the illumination axis. Next, the two cropped distortion-free images are merged at the same location based on the bright-field image. Alternatively, if the images did not have observable distortion, we aligned the single-illumination images based on the profile features and the bright-field image of the sample. Next, we spatially overlapped the two images. For each pixel, we selected the value with the larger Brillouin shift, and inserted it into a new fused data set. The final image was obtained by cropping the region of interest of the fused data set.

Characterization of the dLSBM set-up

To characterize the spectral performance, water at room temperature was used as the standard sample unless stated otherwise (Extended Data Fig. 4). For shot noise experiments, the laser power was ~250 mW, and the acquisition time was tuned between 100 ms and 800 ms to adjust the input light energy. Brillouin signals at each light energy were repeatedly recorded. The signal-to-noise ratio was calculated as the ratio of the average peak intensity and the standard deviation. The measured data were then fitted using a first-order polynomial under a log–log scale. To measure the spectral resolution, the spectra of the laser line were recorded, and the full width at half maximum was quantified. To measure the spectral precision, the measured spectra were fitted using a Lorentzian function, and the standard deviation of the peak position was quantified. For biomedical experiments, the light dose, acquisition time and spectral precision are closely related. Generally, the acquisition time is determined such that the expected spectral precision can be achieved with a light dose that does not cause photodamage.

To characterize the spatial resolution we first measured the transition of the polydimethylsiloxane (PDMS)–water interface, which provides us with the lateral resolution of the set-up (Extended Data Fig. 6a). We then measured the Rayleigh scattering of a 0.5 μm bead (TetraSpeck Microspheres, Thermo Fisher) as it was scanned across by the laser beam and quantified the axial resolution as well as the lateral resolution (Extended Data Fig. 6b). To prepare the sample, the bead was embedded into 1% agarose solution. The mixture was then injected into an FEP (fluorinated ethylene propylene) tube (Cole-Parmer). After gelation, the agarose cylinder was pushed out from one end of the tube for the experiment.

To quantify the shift gradient caused by the refractive index mismatch, a PDMS sphere with a diameter of ~80 μm was embedded into 1% agarose and mapped using the dLSBM set-up (Extended Data Fig. 3). The PDMS sphere was prepared using the vortex-mixing method[23].

Confocal Brillouin microscopy

A standard confocal Brillouin microscope with 180° scattering geometry was used for validation. The details of the instrument can

be found in previous report[7]. In brief, a 660 nm continuous wave laser (Torus, Laser Quantum) with a power of ~10 mW was used as the light source. The add-on Brillouin module was integrated with a commercial inverted confocal microscope (IX81, Olympus) for 2D and 3D mapping. A two-stage VIPA-based Brillouin spectrometer was used for acquisition of the Brillouin signal. The spectrometer is shot noise limited and has a spectral precision of ~10 MHz. An objective lens with NA = 0.4 (LMPLFLN ×20, Olympus) was used for spheroid imaging, and an EMCCD (iXon, Andor) was used for Brillouin signal acquisition with a speed of 50 ms per pixel.

dLSBM and confocal Brillouin microscopy

To verify that dLSBM can capture equivalent mechanical features of the spheroid to those of confocal Brillouin microscopy (CBM), the same spheroid sample was measured by the two set-ups (Extended Data Fig. 7). Given that the two set-ups are in different locations in the laboratory, the spheroid was first measured using dLSBM and then transferred to the CBM set-up. For histogram comparison, the Brillouin shifts of all pixels for each image were plotted, and the histogram was then fitted with a linear combination of two Gaussian distributions. The value of the fitted peak then represents the average Brillouin shift of each group[24].

To investigate the mechanical features of the spheroid on the subcellular level, we stained the nuclei with Hoechst 33342 (Thermo Fisher) and collected the co-registered fluorescence and Brillouin images using the CBM set-up. We then extracted the Brillouin shift of the nucleus region and compared it with the histogram plot based on only Brillouin shift (described above).

Cell culture

MCF10A (M1) and MCF10AT1k.cl2 (M2) cells were received from the Barbara Ann Karmanos Cancer Institute in the United States. They were cultured according to the supplier's protocol, and early passages were cryopreserved and thawed as needed. All cells used were from less than 15 passages. Cells were cultured in T25 flasks at 37 °C, 5% CO_2, in complete medium consisting of DMEM/F12 (11330-032, Thermo Fisher Scientific), 5% horse serum (16050-122, Thermo Fisher Scientific), 5 ng ml^{-1} EGF (AF-100-15-1MG, Peprotech), 0.5 mg ml^{-1} hydrocortisone (H0888-1G, Sigma-Aldrich), 100 ng ml^{-1} cholera toxin (C8052-2mg, Sigma-Aldrich), 10 µg ml^{-1} insulin (I1882-100MG, Sigma-Aldrich) and 1x penicillin–streptomycin solution (15070-063, Thermo Fisher Scientific). Cells were passaged at around 80% confluency using 0.05% trypsin (25-052-Cl, Corning) for 5 min. After treatment with trypsin the cells were centrifuged at 150 ×g for 5 min, resuspended in fresh medium, and seeded in a new T25 flask. Cell medium was changed every 2–3 days.

Spheroid morphogenesis assay in 3D on-top Matrigel culture

Previously established protocols to form acinus-like spheroids of M1 and M2 cells in 3D on-top culture were followed[25,26]. The spheroids were cultured in two-well glass bottom imaging slides (Ibidi, 80287). A total of 200 µl ice-cold Matrigel (Corning, 356231) was added to the well of an imaging slide that was previously chilled on ice. After spreading the Matrigel evenly on the bottom of the well with a pipette tip, the slide was placed in the incubator for 30 min for the layer of Matrigel to solidify. Cells were collected with trypsin from the flask as described above. After centrifugation, the supernatant was aspirated, fresh medium was added, and cells were mixed thoroughly with a pipette to ensure a single-cell suspension. Next, the cells were counted using a hemocytometer. A total of 20,000 cells were carefully mixed in 500 µl of the assay medium. The assay medium was identical to the complete medium except that it contained only 2% horse serum. After that, 500 µl of the cell solution was added on top of the Matrigel layer in the well of a two-well slide. The slide was placed in the incubator for 30 min to allow for the cells to settle on top of the Matrigel layer.

After that, 500 µl assay medium containing 10% Matrigel was carefully pipetted on top of the cells in the well. This yielded a final concentration of 5% Matrigel in assay medium. Acinus-like spheroids will form by day 5 of growth. The medium in the well was changed every 2 days by carefully aspirating the medium and replacing it with a 1 ml solution of 5% Matrigel in assay medium.

Sample preparation for Brillouin imaging

The spheroid sample was collected from the culture dish by gently dislodging the spheroids from the Matrigel in the well with a pipette tip and transferring them to an Eppendorf tube with a pipette. After 5–10 s of centrifuging with a tabletop centrifuge (VWR, Mini Centrifuge), most of the supernatant was removed, and the remaining spheroids at the bottom of the Eppendorf tube were resuspended in 100 µl of a 1% agarose PBS solution that had been warmed to ~37 °C. The solution was carefully pipetted a few times to ensure an even distribution of the spheroids. The solution was then injected into an FEP tube with an internal diameter of 1/16 inches (Cole-Parmer). After allowing 5 min for agarose gelation at room temperature, the agarose gel cylinder containing the embedded spheroids was partially pushed out from the tube using a pipette tip. For the dLSBM experiment, the tube was mounted on the 4D stage, and the gel cylinder was immersed in the PBS solution of the cuvette. For the CBM experiment, the tube along with the gel cylinder was placed into a glass bottom petri dish containing PBS solution.

To perform the osmotic shock experiments, we replaced the medium in the cuvette with a hyperosmotic solution (500 mM sucrose), or a hypoosmotic solution (25% PBS, 75% dH$_2$O). We immersed the spheroids embedded in the agarose gel directly into the solution and proceeded to acquire a time series of Brillouin shift maps.

Photodamage experiment

On day 0, cells were seeded in two-well slides with a 500 µm grid on the bottom (Ibidi) as described above. On day 2 the spheroids in the well (without dislodging them) were placed on the microscope stage, and individual spheroids and their locations on the annotated 500 µm grid were recorded. We illuminated the spheroids with 780 nm light, 370 mW, for 5 min (considering that the typical illumination time is ~3 min for 3D mapping), using the same objective that was used to create the illumination beam in the Brillouin line scan experiments (×4/NA 0.1, Olympus).

To estimate cell viability at the end of the experiment, all spheroids in the well were stained with 2 µM calcein AM, and 5 µM ethidium homodimer-1 (Live/Dead Viability/Cytotoxicity kit, Thermo Fisher Scientific) in PBS for 45 min. The sample was then washed with PBS and imaged using a confocal microscope (Olympus FV3000) with a ×10/0.4 NA objective (UPLSAPO10X2, Olympus). Calcein AM fluorescence was observed in the green channel (488 nm excitation, 500–540 nm emission), and ethidium homodimer was observed in the red channel (514 nm excitation, 590–690 nm emission). A negative control was used to calibrate the fluorescence intensity of the red channel. To prepare the sample of dead spheroids, we removed the medium and added −20 °C methanol for 15 min. The sample was then stained and imaged in the same way as described above. We collected z-stacks (1.4 µm pixel size in the x–y plane, 3.9 µm step in the z direction) for each sample. The maximum intensity projection image of each spheroid was outlined in the green channel, and the average fluorescence intensity of the outlined region was calculated for both the green and red channels with the image processing software Fiji.

To estimate the rate of spheroid growth, we tracked spheroids based on their location on the 500 µm annotated grid. We recorded ×10/0.1 NA bright-field images of the illuminated and control spheroids on each day until day 5. The projected area of the spheroid was manually selected in Fiji. The area versus day data were fitted using an exponential growth model $A = A_0 e^{kt}$ (Prism 8, GraphPad), where A is

the spheroid projected area, A_0 is the initial area, k is the growth rate and t is the time in days. The doubling time was calculated as $\ln(2)/k$. The difference between the doubling time of illuminated and control spheroids was tested using an unpaired, two-tailed t-test with Welch's correction (Prism 8, GraphPad).

Cell and spheroid stiffness measurement using atomic force microscopy

Cell and spheroid stiffness was measured using the NanoWizard 4a atomic force microscope (JPK Instruments). The atomic force microscope (AFM) cantilever with a 5 μm diameter round tip was used for indentation (CP-qp-CONT-Au-B, Nano and More). The spring constant of the cantilevers was calibrated using the thermal noise method while they were immersed in the cell medium in the dish. For measurement of single cells, cells suspended in 2 ml assay medium were added to the glass bottom dish (FluoroDish, World Precision Instruments) and allowed to settle for 2 min on the glass bottom. The tip was centered on the cell body and each cell was indented with the maximum force setpoint of 5 nN and an approach speed of 2 μm s⁻¹ across the height range of 5 μm. The measurement was repeated nine times in the same location and each indentation curve was recorded. For spheroid measurements on day 5 of growth, the spheroids were physically detached from the Matrigel bottom layer in the well with a pipette tip and transferred to an Eppendorf tube. They were centrifuged for 5–10 s using the tabletop centrifuge, and supernatant that may contain chunks of Matrigel was removed. Spheroids were then carefully resuspended in 2 ml assay medium and added to a glass bottom dish. After they were allowed to settle for 2 min, the AFM tip was centered on each spheroid and indented nine times in the same location with the maximum force setpoint of 25 nN, with an approach speed of 2 μm s⁻¹ across the height range of 15 μm. The height of the spheroids was measured by bringing the AFM tip to the top of the spheroid using a 1 nN setpoint and recording the tip height. For each spheroid, we also recorded the tip height when the tip contacted the glass bottom near the same spheroid. The AFM indentation curves were analyzed using the JPK data processing software. Indentation curves were fitted using Hertz models on the 75% of the curve (that is, the initial 25% of the force-distance curve was removed from the fit to avoid artifact due to uneven approach of the tip to the sample), assuming a Poisson ratio of 0.5 and a spherical indenter with a diameter of 5 μm. For each cell or spheroid, the Young's modulus from all nine indentation measurements was averaged. At least five cells or spheroids were measured in each condition, and each experiment was repeated three times. Statistical differences were tested using the unpaired, two-tailed t-test with Welch's correction (Prism 8, GraphPad).

Reporting summary

Further information on research design is available in the Nature Portfolio Reporting Summary linked to this article.

Data availability

The authors declare that all data supporting the findings of this study are available in the paper and its Supplementary Notes 1 and 2. Source data are provided with this paper.

Code availability

The MATLAB codes for spectrum analysis and image fusion are provided as Supplementary Codes 1 and 2 software under MIT license.

References

23. Schlüßler, R. et al. Correlative all-optical quantification of mass density and mechanics of subcellular compartments with fluorescence specificity. *eLife* **11**, e68490 (2022).
24. Zhang, J., Nou, X., Kim, H. & Scarcelli, G. Brillouin flow cytometry for label-free mechanical phenotyping of the nucleus. *Lab Chip* **17**, 663–670 (2017).
25. Lee, G. Y., Kenny, P. A., Lee, E. H. & Bissell, M. J. Three-dimensional culture models of normal and malignant breast epithelial cells. *Nat. Methods* **4**, 359–365 (2007).
26. Debnath, J., Muthuswamy, S. K. & Brugge, J. S. Morphogenesis and oncogenesis of MCF-10A mammary epithelial acini grown in three-dimensional basement membrane cultures. *Methods* **30**, 256–268 (2003).
27. Schlüßler, R. et al. Mechanical mapping of spinal cord growth and repair in living zebrafish larvae by Brillouin imaging. *Biophys. J.* **115**, 911–923 (2018).

Acknowledgements

Author contributions

J.Z. and G.S. conceived the project. J.Z., M.N., K.T. and G.S. devised the research plan. J.Z. developed the instrument and performed the experiments. M.N. developed the spheroid protocols and performed the photodamage experiment and AFM measurement. J.Z. and G.S. wrote the manuscript with input from all of the other authors.

Competing interests

J.Z., M.N and G.S. are inventors of patents related to the Brillouin technology. G.S. is a consultant for Intelon Optics. K.T. declares no competing interests.

Additional information

Extended data are available for this paper at https://doi.org/10.1038/s41592-023-01816-z.

Supplementary information The online version contains supplementary material available at https://doi.org/10.1038/s41592-023-01816-z.
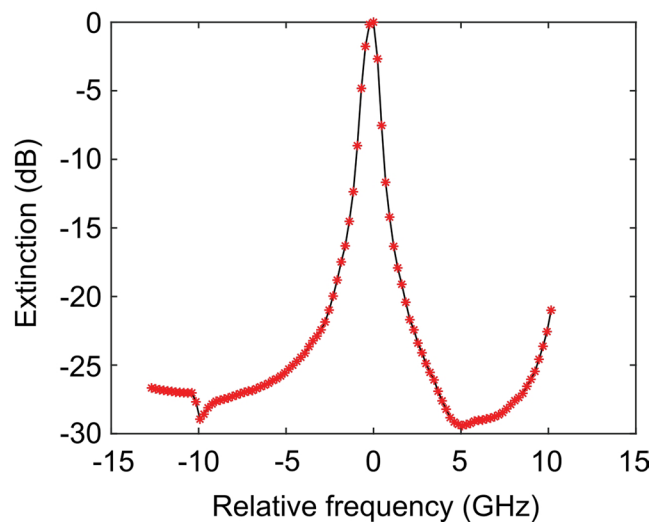
Correspondence and requests for materials should be addressed to Jitao Zhang or Giuliano Scarcelli.

Peer review information *Nature Methods* thanks the anonymous reviewers for their contribution to the peer review of this work. Peer reviewer reports are available. Primary Handling Editor: Nina Vogt, in collaboration with the *Nature Methods* team.

Reprints and permissions information is available at www.nature.com/reprints.

a

b

c
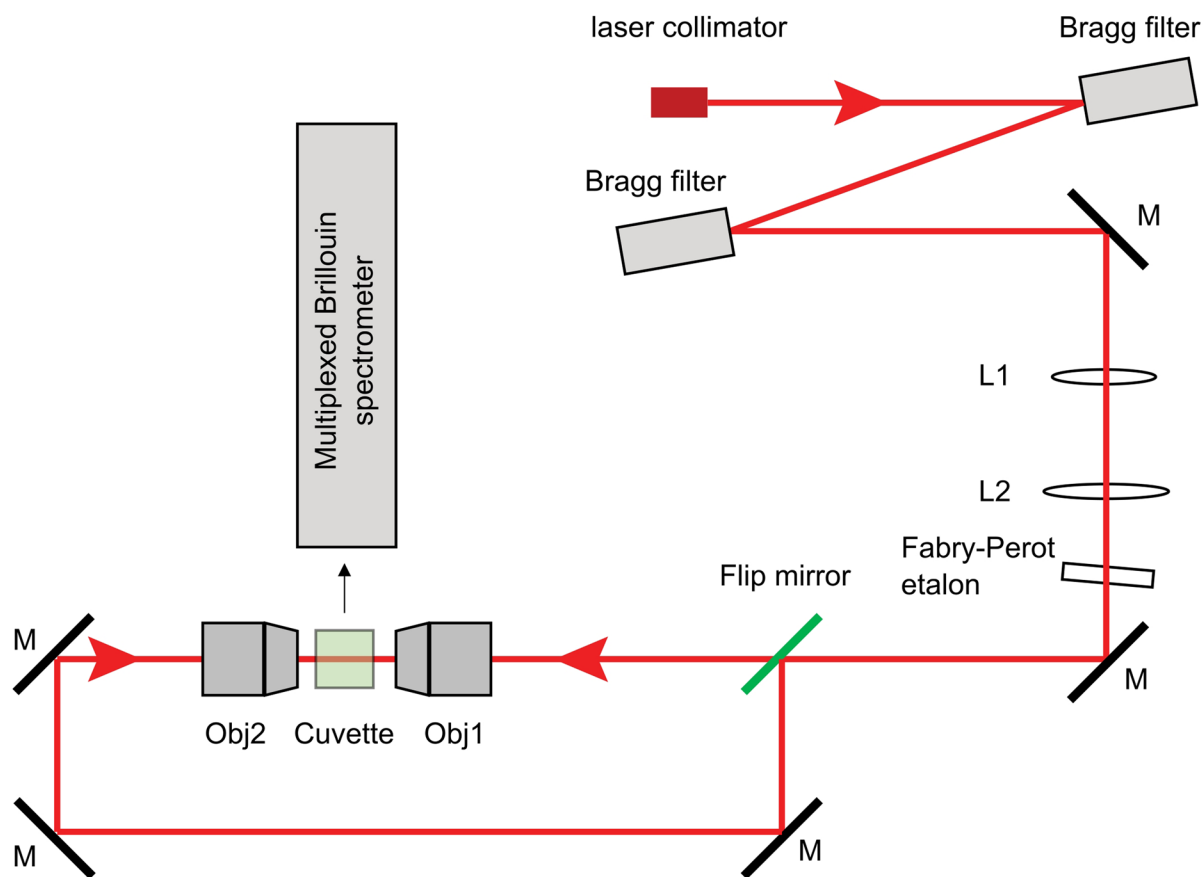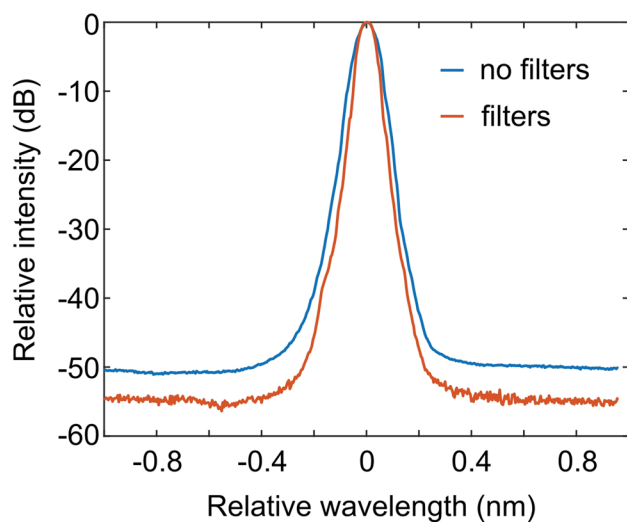
Extended Data Fig. 1 | Detailed schematic of the illumination beam. a, M, mirror; L1-L2, spherical lens with focal length of 20 mm and 80 mm, respectively; Obj1-Obj2, objective lenses (4×/0.1NA). **b**, Measured laser spectra with and without Bragg filters. **c**, Extinction spectrum of the Fabry-Perot etalon used in the setup. The value of zero in **b** and **c** represents the wavelength and frequency of the laser light, respectively.

a

b

c
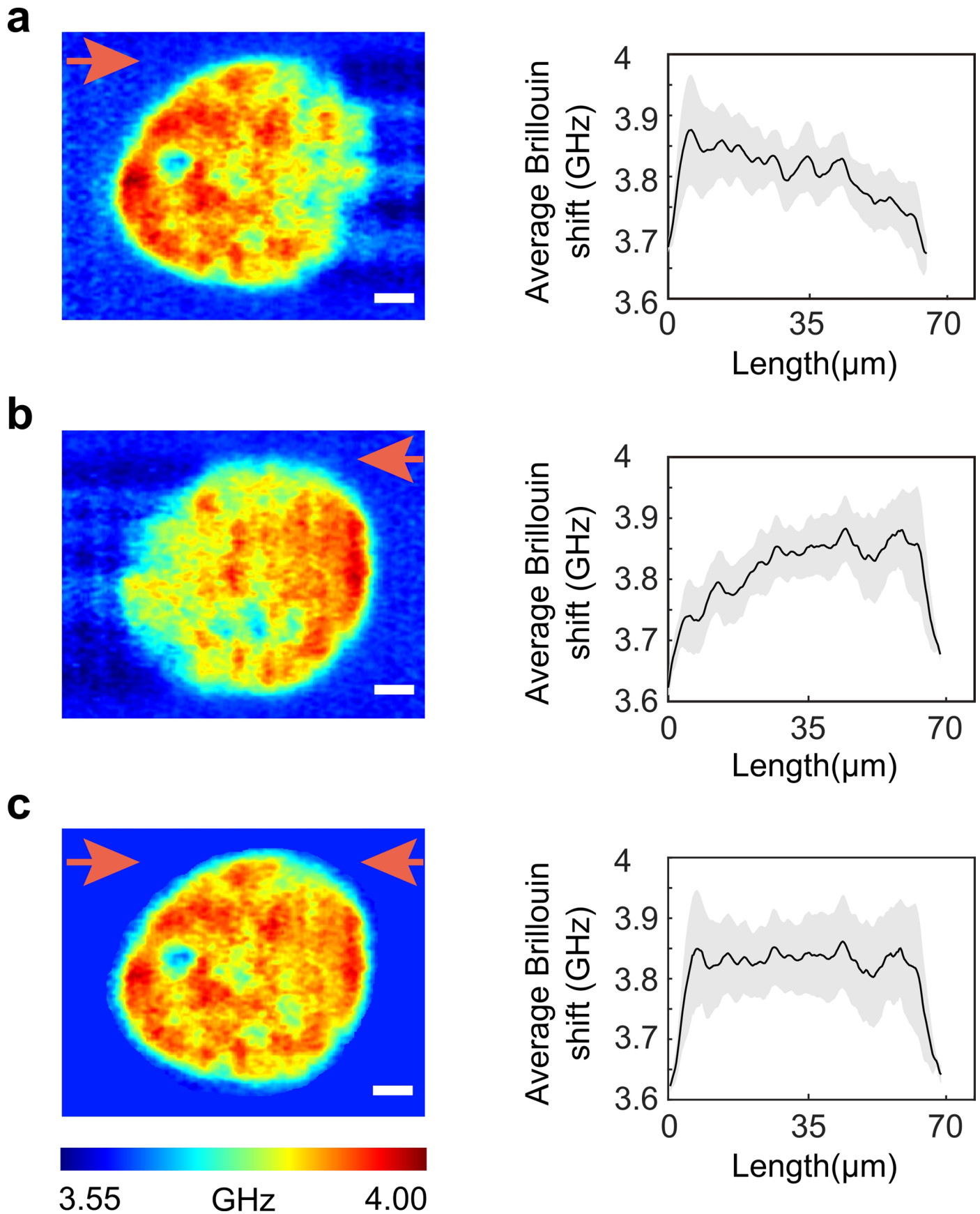
Extended Data Fig. 2 | Dual-line illumination. Brillouin image sections (left panels) and the averaged profile (right panels) along illumination direction of left-line illumination (**a**), right-line illumination (**b**), and combined dual-line illumination (**c**). The red arrow indicates the illumination direction of the beam line. Scale bar, 10 μm. The color bar represents the Brillouin shift with the unit of GHz. The center and error band represents the mean value +/− SD.

a

b

c

d
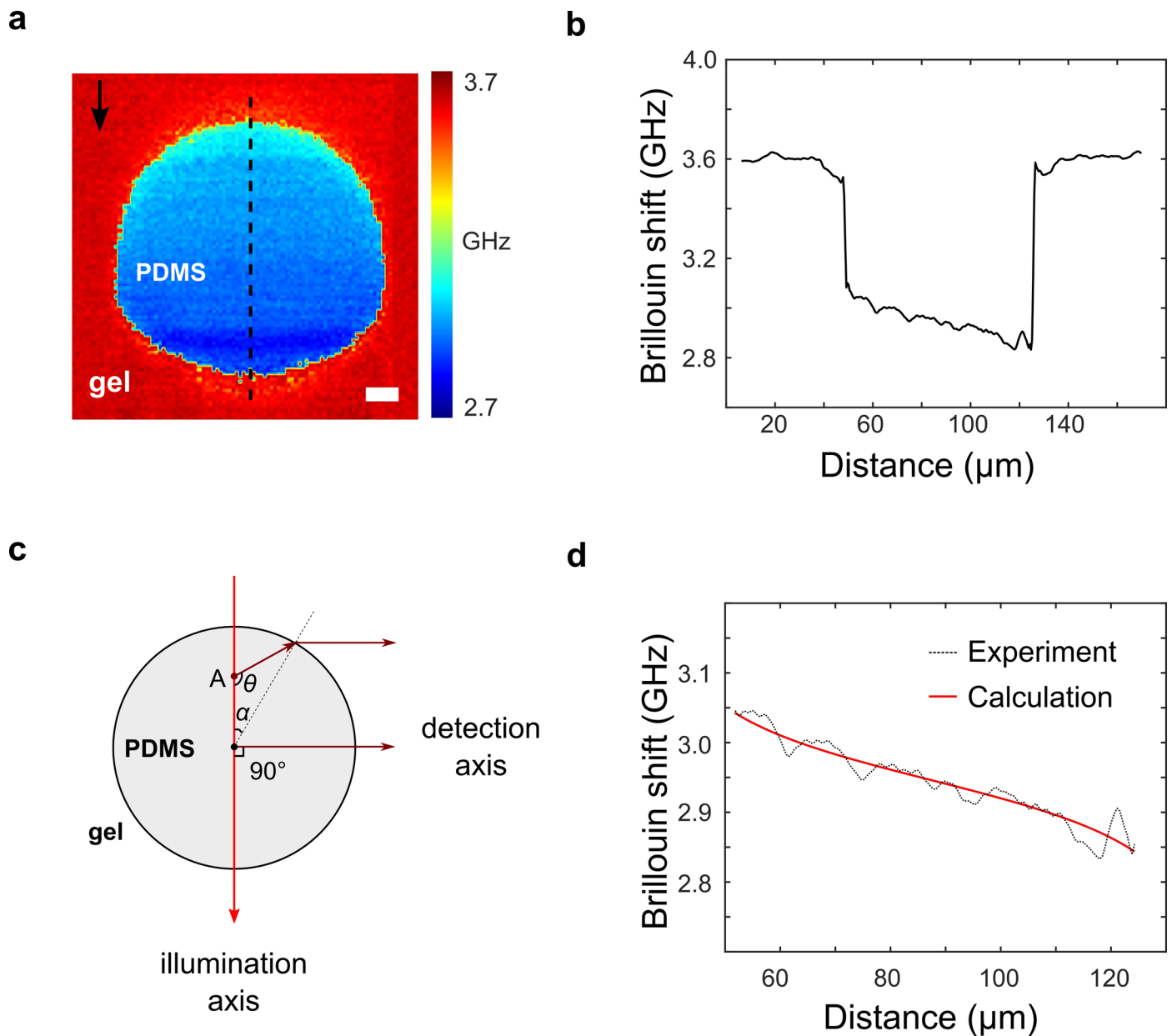
Extended Data Fig. 3 | Brillouin shift gradient caused by the mismatch of refractive index. a, Brillouin image of a PDMS sphere immersed in 1% agarose gel. Arrow indicates the propagation of illumination beam. Black dashed line indicates the location of interest for **b**. Scale bar is 10 μm. **b**, Shift profile across the PDMS sphere shows the gradient along illumination direction. **c**, Theoretical calculation model. 'A' represent an arbitrary point on the illumination axis, θ is the actual scattering angle collected by the spectrometer at 90° geometry, and α is the azimuthal angle of the sphere. **d**, The shift gradients from the calculation and the experiment.
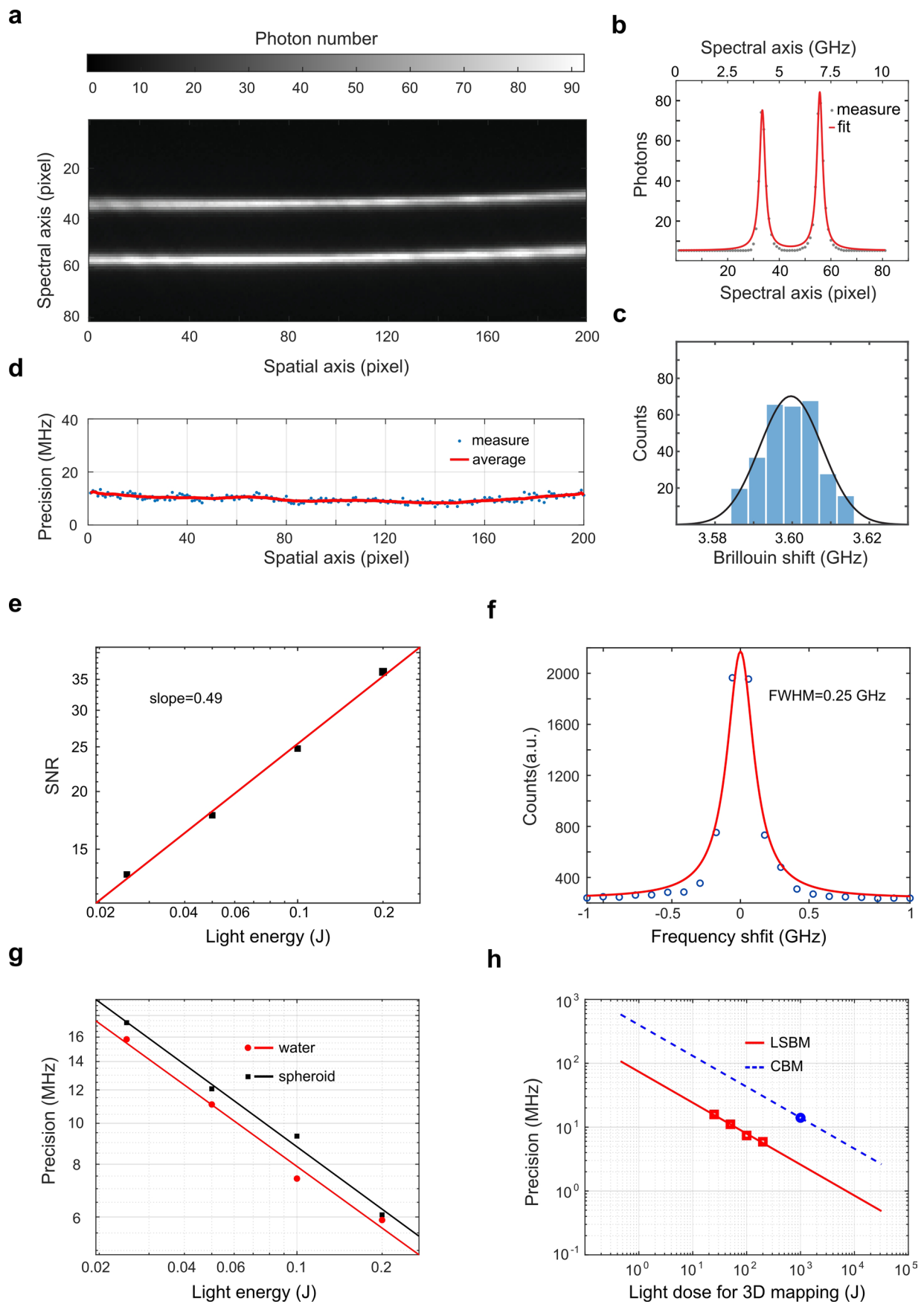
Extended Data Fig. 4 | See next page for caption.

Extended Data Fig. 4 | Characterization of Brillouin spectrometer.
a, Exemplary raw Brillouin spectrum of DI water acquired by the spectrometer of the dLSBM setup with single-line illumination. **b**, Brillouin shift is extracted by fitting the spectrum of a single pixel with a Lorentzian function. Peaks represent the Stokes and anti-Stokes components of the Brillouin frequency.
c, Representative histogram distribution of the estimated Brillouin shift of the same point after repeated acquisition (n = 300). The solid line is fitting result by Gaussian profile. The standard deviation of the estimated Brillouin shift is 8 MHz.
d, Spectral precision of all points on illumination axis. The average is 9.8 MHz.

e, Signal-to-noise (SNR) ratio against light energy of dLSBM spectrometer for water sample. The fitted line has a slope of 0.49.**f**, The measured spectrum of the laser. Circles are measured data, and solid line is Lorentzian fit. **g**, Spectral precision against light energy of the dLSBM spectrometer in water and spheroid sample. **h**, Comparison of dLSBM and confocal Brillouin microscopy (CBM) regarding the spectral precision against total light dose for 3D mapping of $100 \times 200 \times 10$ pixels. water is used as sample. The data point of CBM is adapted from ref. [27], and the dash line indicates the shot noise limited operation.
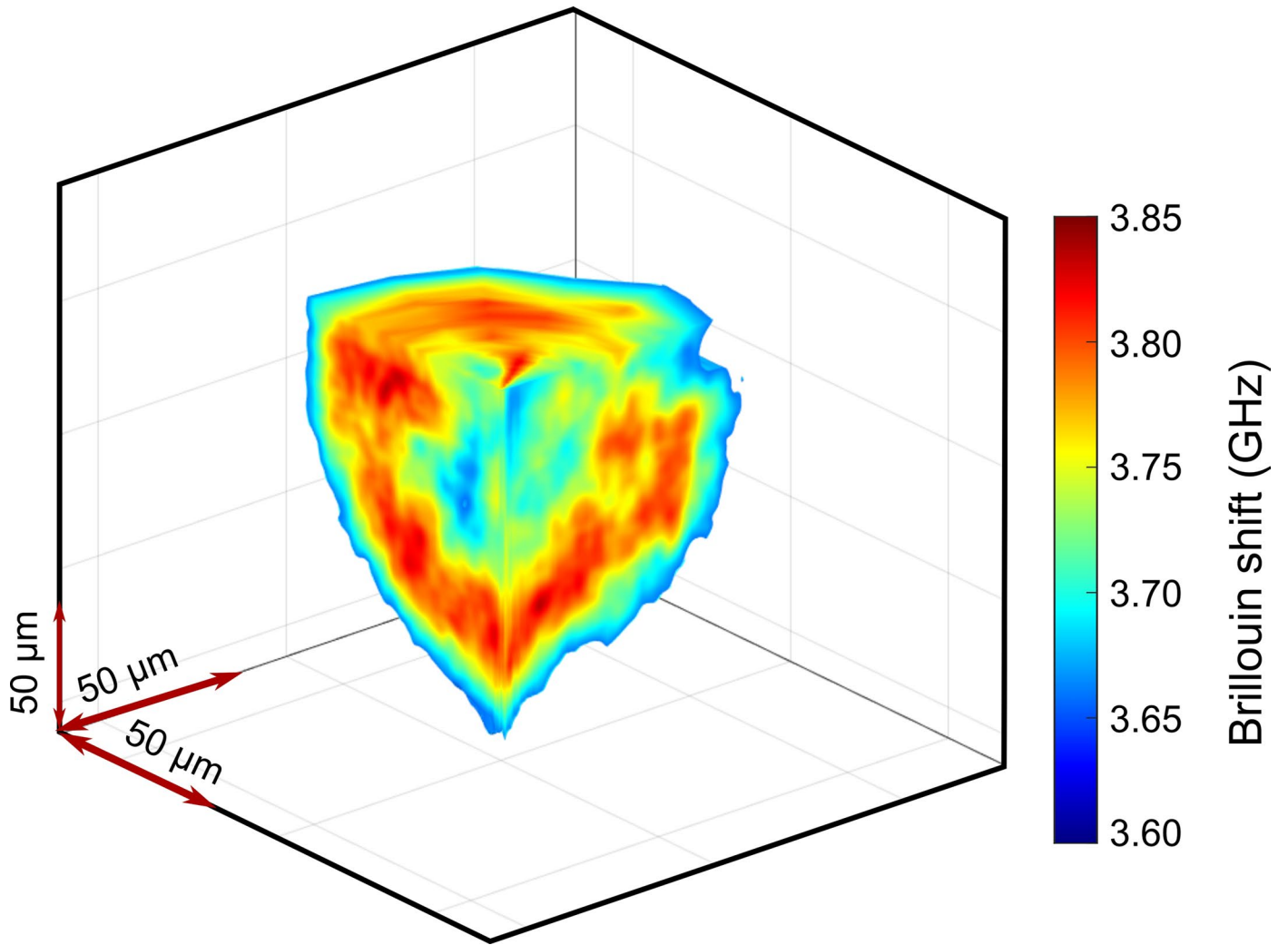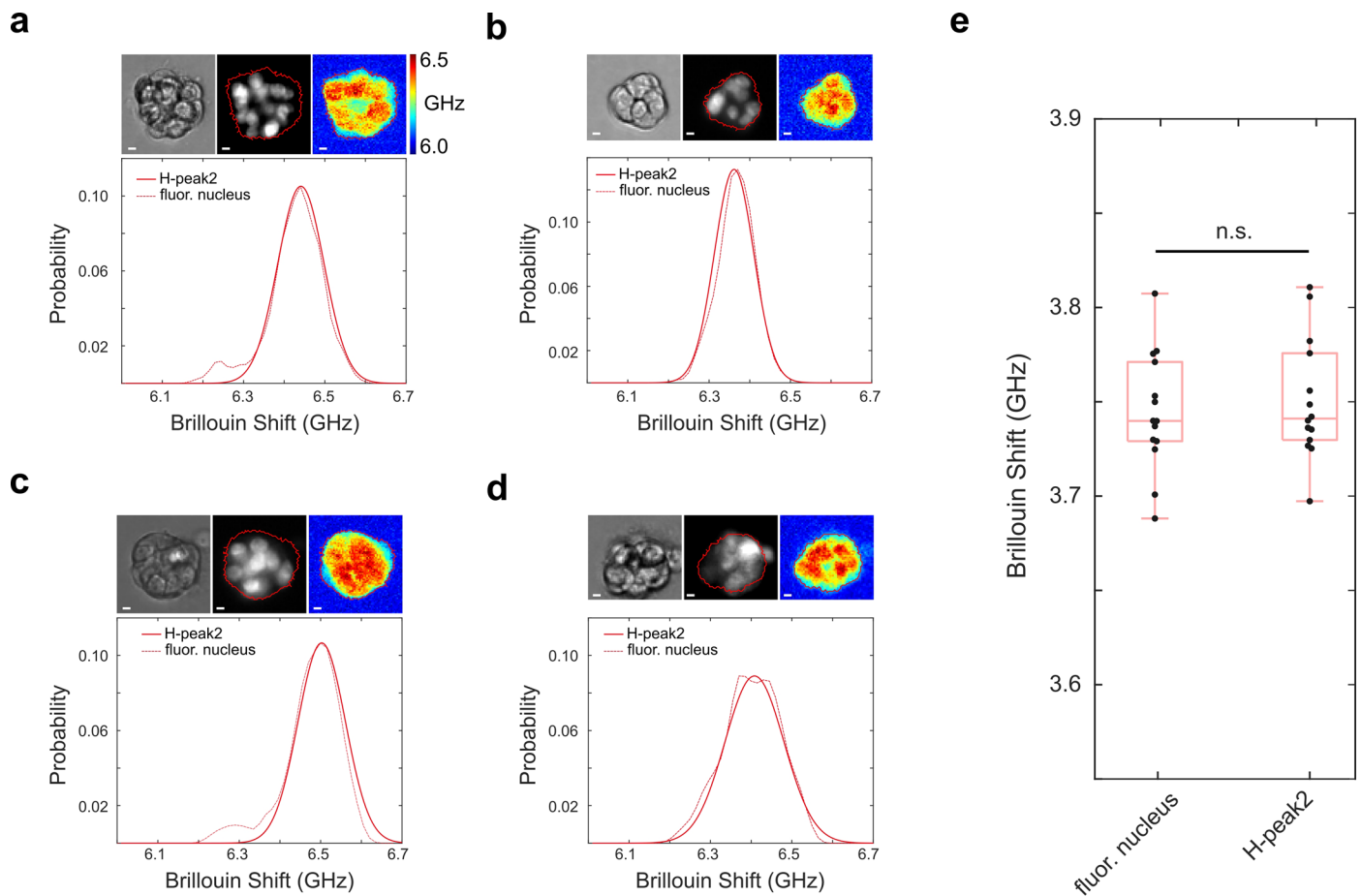
Extended Data Fig. 5 | Brillouin image reconstruction of the 3D mapping of a spheroid.

a

b
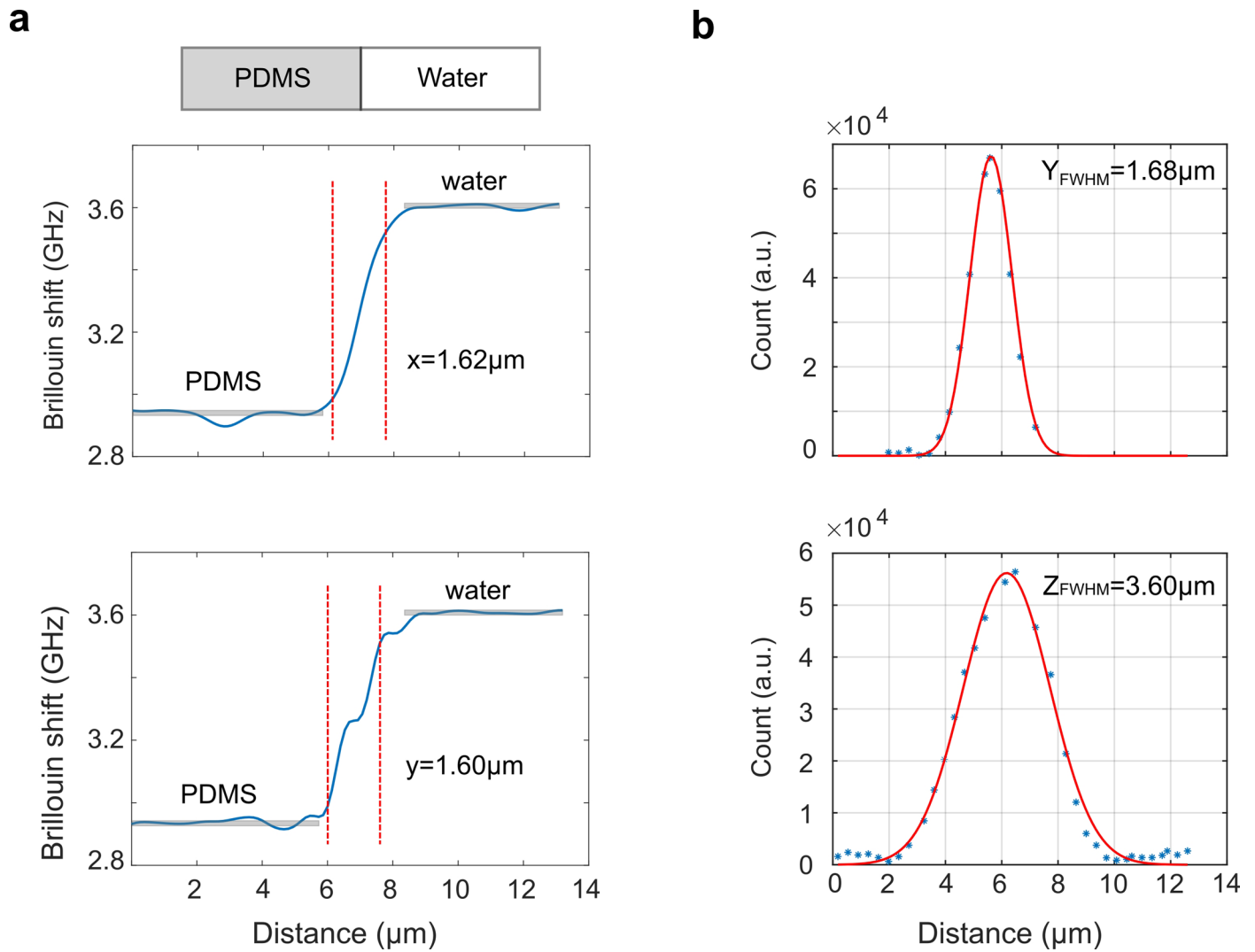
Extended Data Fig. 6 | Characterization of the spatial resolution of the dLSBM setup. a, Brillouin measurement across the interface of PDMS and water. **b**, Measurement of Rayleigh scattering from a 0.5 μm bead.
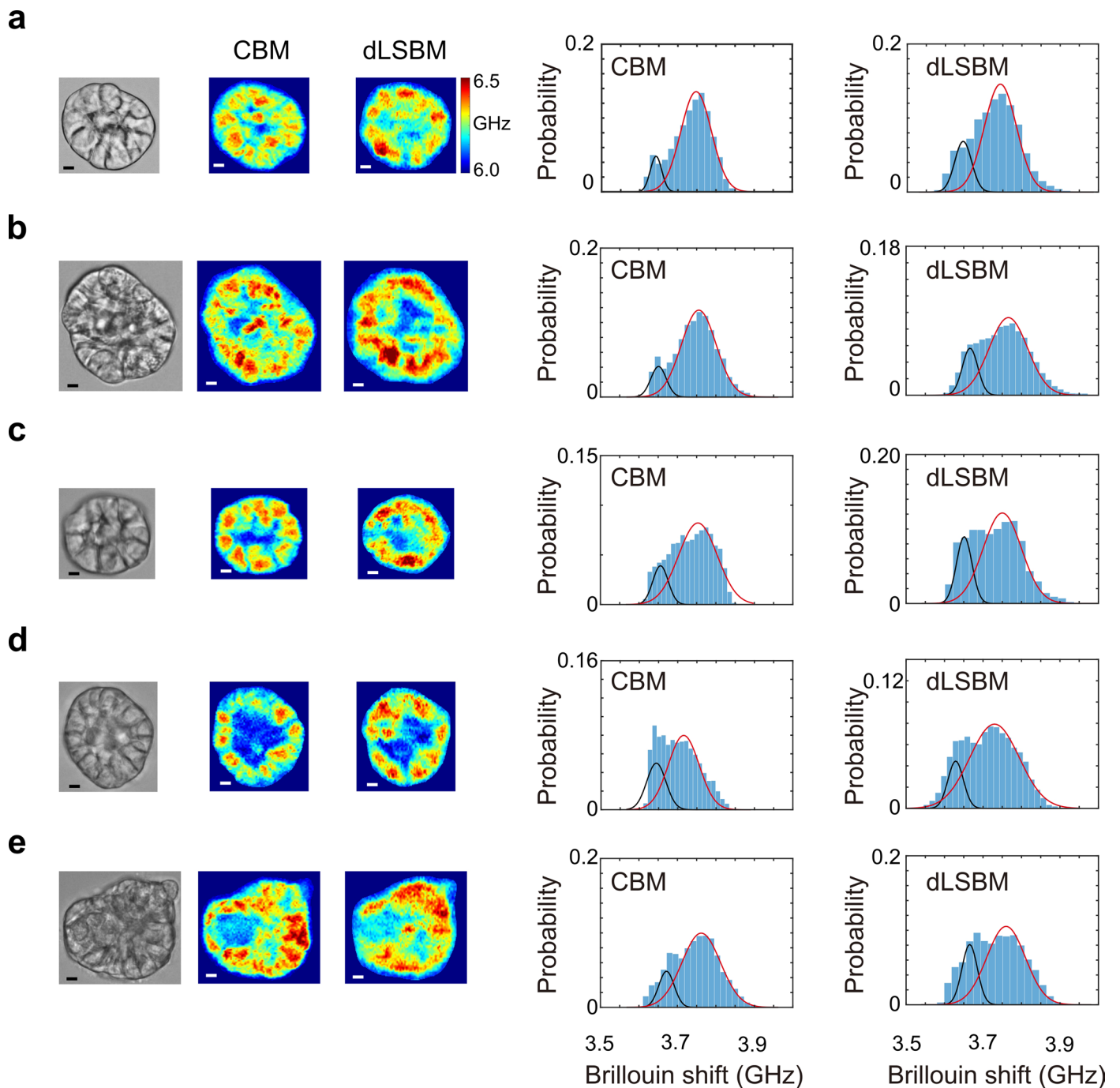
Extended Data Fig. 7 | Comparison of dLSBM and CBM. a-e, five independent spheroids measured by dLSBM (NA = 0.3) and CBM (NA = 0.4). Scale bar is 5 μm. For each spheroid, the Brillouin shifts of all pixels from the image was plotted into a histogram. The histogram was then fitted by a combination of two Gaussian distributions.

Extended Data Fig. 8 | Analysis of subcellular mechanical information of spheroids. a-d, Co-registered fluorescence and Brillouin images of four representative spheroids. Each sub figure shows the bright field image, fluorescence image of the nuclei, and the Brillouin image acquired by the CBM, respectively. Red line in the image outlines the profile of the spheroid. The plots of 'H-peak 2' is the right peak extracted from the curve fitting of the Brillouin shift histogram. The plots of 'fluor. nucleus' represents Brillouin shift of the nucleus region. **e,** Results of all the spheroid samples (n = 14). n.s.: not statistically significant (*p* = 0.6039). Statistical significance is determined by performing two-sided two-sample t-test, and no adjustment was made. In all boxplots, the central mark indicates the median, and the bottom and top edges indicate the 25th and 75th percentiles, respectively. The whiskers extend to the most extreme data points not considered outliers.
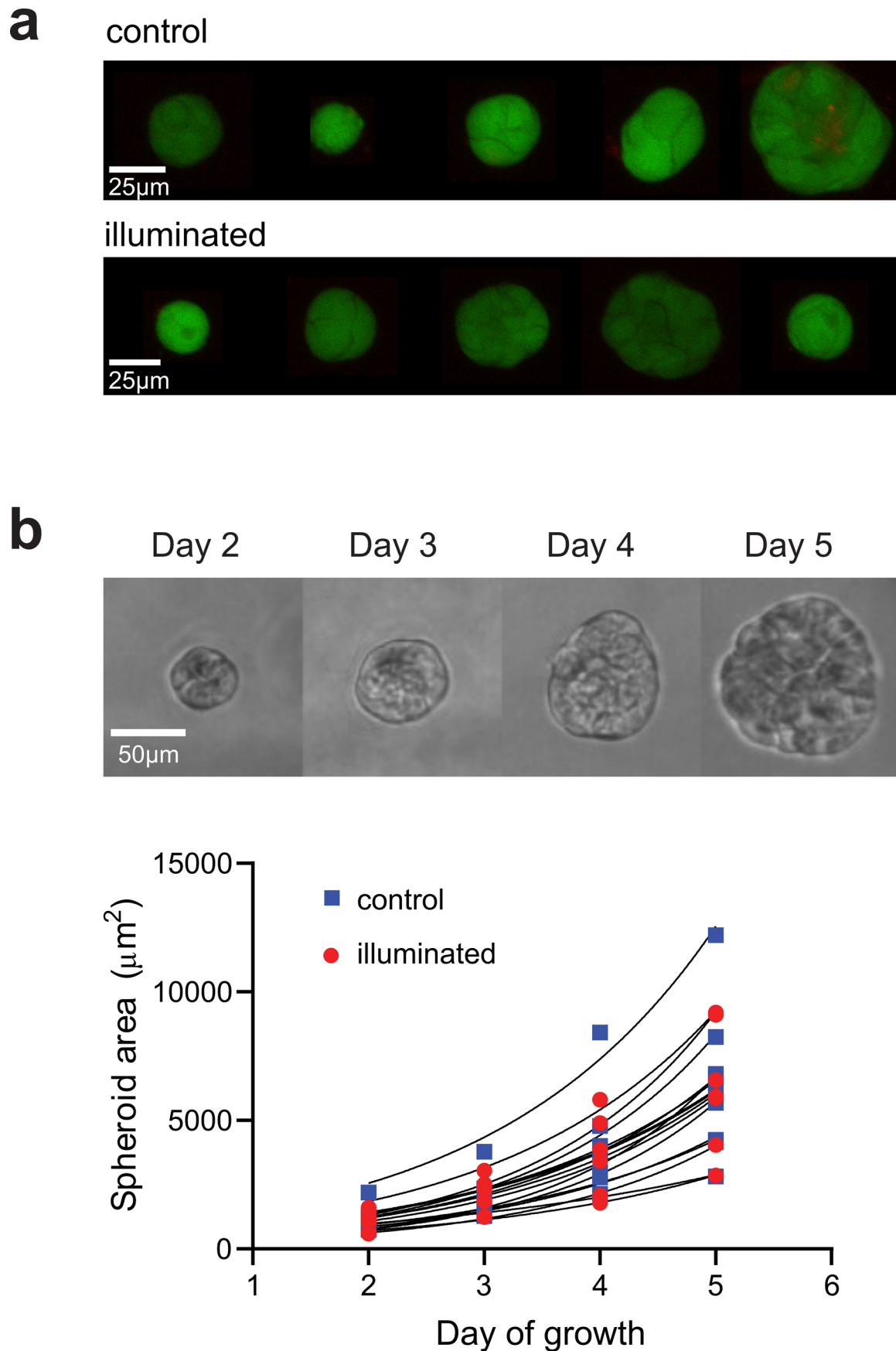
Extended Data Fig. 9 | Effect of light illumination on the viability and growth rate of the spheroids. a, Fluorescent images of the spheroids in control and illuminated groups. Live cells fluoresce in green (Calcein-AM) and dead cells fluoresce in red (EthD-1). **b**, Spheroid area against day of growth. The upper panel is the representative time-lapse image of a spheroid that is illuminated on Day 2. The points in the lower panel represent the area of spheroids over time. Black curves are best fit for exponential growth. Control group (n = 10), Illuminated group (n = 7).
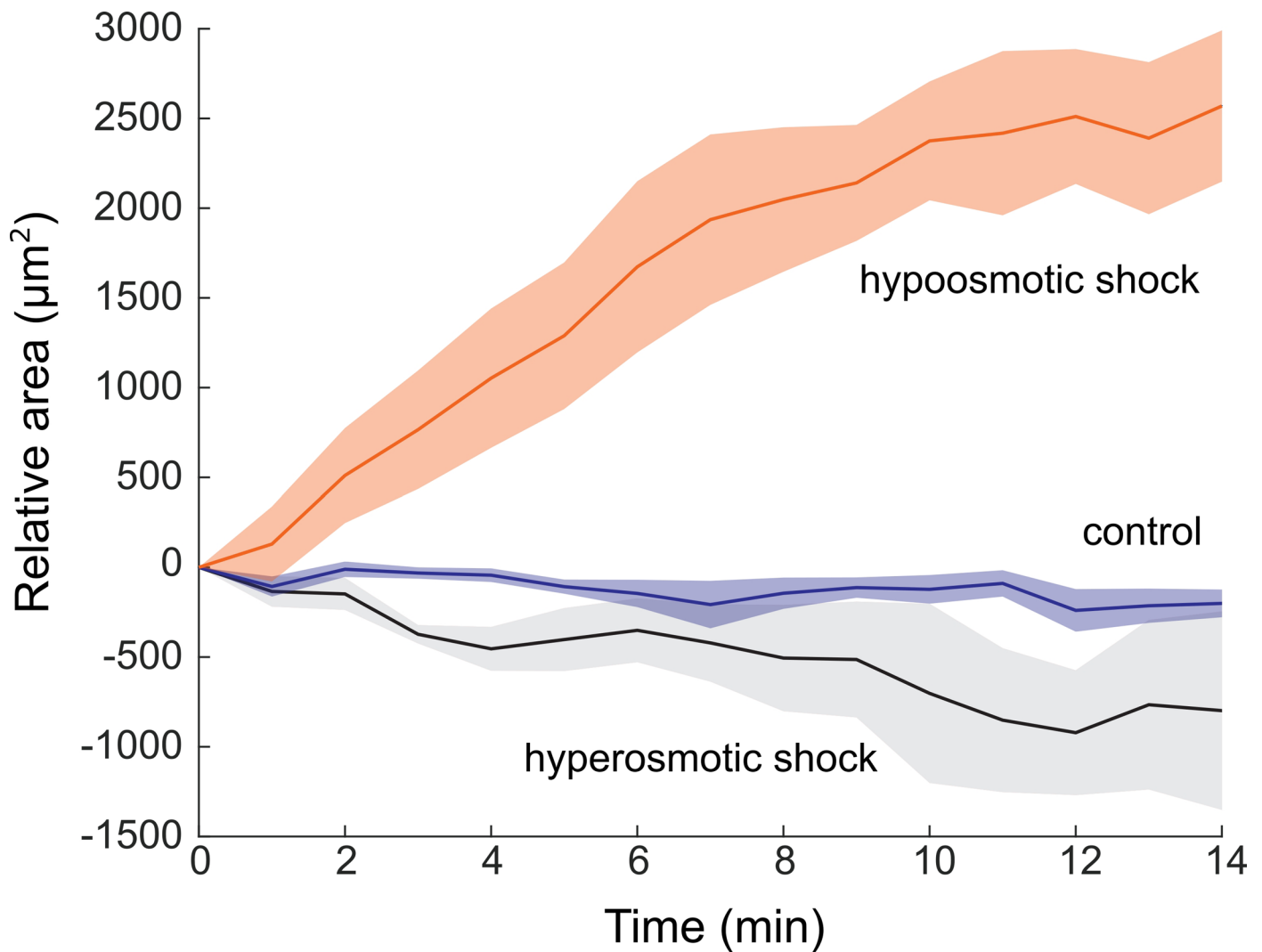
Extended Data Fig. 10 | Temporal change of the projection area of the spheroids under osmotic shock. Hyperosmotic shock (n = 5), no shock (n = 6), and hypoosmotic shock (n = 5). Error bound indicates ± s.e.m.

Corresponding author(s): Jitao Zhang, Giuliano Scarcelli

Last updated by author(s): Dec 3, 2022

Reporting Summary

Nature Portfolio wishes to improve the reproducibility of the work that we publish. This form provides structure for consistency and transparency in reporting. For further information on Nature Portfolio policies, see our Editorial Policies and the Editorial Policy Checklist.

Statistics

For all statistical analyses, confirm that the following items are present in the figure legend, table legend, main text, or Methods section.

n/a	Confirmed	
☐	☒	The exact sample size (n) for each experimental group/condition, given as a discrete number and unit of measurement
☐	☒	A statement on whether measurements were taken from distinct samples or whether the same sample was measured repeatedly
☐	☒	The statistical test(s) used AND whether they are one- or two-sided *Only common tests should be described solely by name; describe more complex techniques in the Methods section.*
☒	☐	A description of all covariates tested
☒	☐	A description of any assumptions or corrections, such as tests of normality and adjustment for multiple comparisons
☐	☒	A full description of the statistical parameters including central tendency (e.g. means) or other basic estimates (e.g. regression coefficient) AND variation (e.g. standard deviation) or associated estimates of uncertainty (e.g. confidence intervals)
☐	☒	For null hypothesis testing, the test statistic (e.g. F, t, r) with confidence intervals, effect sizes, degrees of freedom and P value noted *Give P values as exact values whenever suitable.*
☒	☐	For Bayesian analysis, information on the choice of priors and Markov chain Monte Carlo settings
☒	☐	For hierarchical and complex designs, identification of the appropriate level for tests and full reporting of outcomes
☒	☐	Estimates of effect sizes (e.g. Cohen's d, Pearson's r), indicating how they were calculated

Our web collection on statistics for biologists contains articles on many of the points above.

Software and code

Policy information about availability of computer code

Data collection	Brillouin shift in samples was imaged using the line-scan Brillouin microscope (see methods) which was controlled by a custom built LabVIEW ver.2021 program.
Data analysis	Spectral data was analyzed using custom scripts written in Matlab R2021b or later version. Image analysis was performed using a combination of Fiji (version 2.1.0/1.53c) and Matlab, and statistical analysis was performed in GraphPad Prism 8 (see methods). AFM indentation data was processed using the JPK data processing software v6 provided by Brucker, the instrument manufacturer. Matlab code examples for spectrum analysis and image fusion are provided as Supplementary code.

For manuscripts utilizing custom algorithms or software that are central to the research but not yet described in published literature, software must be made available to editors and reviewers. We strongly encourage code deposition in a community repository (e.g. GitHub). See the Nature Portfolio guidelines for submitting code & software for further information.

Data

Policy information about availability of data

All manuscripts must include a data availability statement. This statement should provide the following information, where applicable:
- Accession codes, unique identifiers, or web links for publicly available datasets
- A description of any restrictions on data availability
- For clinical datasets or third party data, please ensure that the statement adheres to our policy

The authors declare that all data supporting the findings of this study are available within the paper and its Supplementary note files.

Field-specific reporting

Please select the one below that is the best fit for your research. If you are not sure, read the appropriate sections before making your selection.

☒ Life sciences ☐ Behavioural & social sciences ☐ Ecological, evolutionary & environmental sciences

For a reference copy of the document with all sections, see nature.com/documents/nr-reporting-summary-flat.pdf

Life sciences study design

All studies must disclose on these points even when the disclosure is negative.

Sample size	Sample sizes and experimental replication scheme were chosen based on our previous experience, and to be reasonably large to demonstrate the feasibility of the technique for biological application. These choices were based based on the current best practices in the field: see Mahajan, Vaibhav, et al. Cancers 13.21 (2021): 5549. or Nikolić, M., et al. Biophysical Journal 121.19 (2022): 3586-3599.
Data exclusions	No data were excluded from the analysis.
Replication	All replications were successful and gave similar results. All AFM and Brillouin microscopy experiments were repeated independently at least three times (from a fresh culture flask of cells, with fresh aliquots of ingredients). Cell viability and proliferation rate experiments were replicated in multiple spheroids in the same culture well, i.e. in one independent preparation of the cell culture well.
Randomization	All spheroids at certain culturing day, in a given experimental condition were selected at random, in random fields of view during data acquisition. Identical and independent culture wells were prepared for each experimental condition, therefore no special allocation procedure was necessary.
Blinding	Investigators were not blinded during data acquisition and analysis. Blinding was not necessary since data analysis was automated and standardized across all experimental conditions.

Reporting for specific materials, systems and methods

We require information from authors about some types of materials, experimental systems and methods used in many studies. Here, indicate whether each material, system or method listed is relevant to your study. If you are not sure if a list item applies to your research, read the appropriate section before selecting a response.

Materials & experimental systems

n/a	Involved in the study
☒	☐ Antibodies
☐	☒ Eukaryotic cell lines
☒	☐ Palaeontology and archaeology
☒	☐ Animals and other organisms
☒	☐ Human research participants
☒	☐ Clinical data
☒	☐ Dual use research of concern

Methods

n/a	Involved in the study
☒	☐ ChIP-seq
☒	☐ Flow cytometry
☒	☐ MRI-based neuroimaging

Eukaryotic cell lines

Policy information about cell lines

Cell line source(s)	MCF10A cell line was purchased from American Type Culture Collection. MCF10AT1k.cl2 cell line was obtained from Dr. Lisa Polin from Barbara Ann Karmanos Cancer Institute at Wayne State University (Detroid, MI, USA).
Authentication	Cells were not authenticated. Only cells with low passage number (<15) were used after obtaining them directly from the supplier.
Mycoplasma contamination	Prior to the experiments cell lines were tested for mycoplasma with the MycoFluor Mycoplasma Detection Kit (Thermofisher) and were confirmed to be negative for mycoplasma.
Commonly misidentified lines (See ICLAC register)	None.